Received: 4 January 2019 | Revised: 1 April 2019 | Accepted: 12 April 2019

DOI: 10.1111/jace.16504

Journal of the American Ceramic Society

ORIGNAL ARTICLE

Photocurrents in crystal-amorphous hybrid stannous oxide/alumina binary nanofibers

JinKiong Ling[1] | **Pal Bhupender**[1] | **Chong KwokFeng**[1] | **Lukas Schmidt-Mende**[2] | **Juan Bisquert**[3] | **Rajan Jose**[1]

[1]Nanostructured Renewable Energy Material Laboratory (NREML), Faculty of Industrial Sciences & Technology, Universiti Malaysia Pahang, Kuantan, Malaysia

[2]Department of Physics, University of Konstanz, Konstanz, Germany

[3]Photovoltaic and Optoelectronic Devices Group, Departament de F´ ısica, Universitat Jaume I, Castell´o, Spain

Correspondence
Rajan Jose, Nanostructured Renewable Energy Material Laboratory (NREML), Faculty of Industrial Sciences & Technology, Universiti Malaysia Pahang, 26300 Kuantan, Malaysia.
Email: rjose@ump.edu.my

Funding information
Flagship Leap 3, Grant/Award Number: RDU172201

Abstract

Suppression of charge recombination by thin amorphous alumina layers on metal oxide semiconductors has demonstrated a vital role in electronic appliances beside its role as an insulator. This study reports effect of amorphous alumina (Al_2O_3) on the structural, electrical, and optical properties of stannous oxide (SnO_2). The samples for the present study are prepared as nanofibers by electrospinning a polymeric solution containing aluminum and stannous precursors and subsequent annealing; six samples with varying concentrations of aluminum and stannous are considered. A crystal-amorphous SnO_2/Al_2O_3 hybrid system was confirmed by both XRD and XPS analysis. Both BET and Mott-Schottky analysis showed increase in the surface area and conduction band minimum of the sample with increase in the Al content, however, at the expense of its electrical conductivity. The electron lifetime of the sample increased with increase in the Al content, but the electron transport time increase with decrease in the electrical conductivity of the sample. Both Urbach energy measurement and Stoke's shift showed generation of deeper trap state with increase in the Al content. Investigation on sample photovoltaic performance showed that the loss in electrical conductivity of the sample can be compensated by the improved surface area to a certain extent. Interestingly, a composite nanofiber containing equal molar fraction of aluminum and stannous showed orders of magnitude higher photocurrent despite its similar resistivity as that of pure alumina fibers, which is shown to originate from a Fermi energy gradient at the Al_2O_3/SnO_2 interface.

KEYWORDS

Al-doped SnO_2, band bending, composite nanofibers, crystal-amorphous composite, SnO_2/Al_2O_3 composite

1 | INTRODUCTION

Alumina (Al_2O_3) and stannous oxide (SnO_2) are archetypical functional ceramics offering different properties and are in use for a variety of applications due to their structural to electrical properties. The Al_2O_3 crystallize in a variety of polymorphs, viz. α-Al_2O_3, η-Al_2O_3, γ-Al_2O_3, β-Al_2O_3, and amorphous Al_2O_3 (Am-Al_2O_3),[1–3] as a results of difference in crystallization temperature in the range of 600°C-900°C,[3] where a calcination temperature <600°C result in Am-Al_2O_3.[4,5] The electrical properties of Al_2O_3 vary among polymorphs and with crystallinity: Am-Al_2O_3 has an energy gap ~2.6-2.9 eV whereas that of well-ordered α-Al_2O_3 is ~7.0 eV, both with a direct band gap.[6–11] Due to this wide energy gap, well-crystalized Al_2O_3 is resistive[12] and with high conduction band as well as low valence band energies.[8] Although Am-Al_2O_3 has its energy gap in the semiconductor range, it is poorly conductive due to its highly disordered particle distribution. Therefore,

am-Al_2O_3 is mostly used as an insulating material for electrical applications. On the contrary, SnO_2 is well-known for its application as a metal oxide semiconductor (MOS)[13] despite having relatively larger energy gap (~3.6 eV) than other MOS such as TiO_2 (energy gap ~3.2 eV).[14] Due to high conductivity, *n*-type semiconductor behavior, and high optical transparency, SnO_2 is widely applied as transparent conducting electrode in electrical applications.[15] The electronic structure of Al_2O_3 differs among crystal phase due to differing ratios of octahedral/tetragonal orientation of Al atoms in its crystal structure,[8] where higher tetragonal content resulted in larger energy shift of conduction band minimum (CBM). Despite of different energy gaps, Al_2O_3 in different crystal phase has similar valence band maximum, consisting of 2p level of Al atoms.[16] In contrast, conduction band minimum of SnO_2 resulted from hybridization of O-2p and Sn-5s states, where its valence band maximum consists mainly O-2p and Sn-4d states.[17]

Despite having higher conductivity, N-type semiconducting behavior and better optical transparency, both lower surface area and CBM hindered the successful implementation of SnO_2 in high-performance electronic appliances, especially in photovoltaics. Although efforts had been carried out to improve the surface area of SnO_2,[18,19] such improvements only resulted in an increase in photocurrent on dye-sensitized solar cells; the open-circuit voltage (V_{OC}) remain low as usual.[20,21] This issue was overcome by combining a material with higher CBM, for example, developing a thin TiO_2 film on SnO_2,[21] which resulted in improved in charge transport and an upshift in CBM. Sasidharan et al. [22] demonstrated that deposition of compact ZnO layer on SnO_2 improved the electron lifetime by suppressing charge recombination, thereby improving DSSC's photocurrent, V_{OC}, and efficiency. Besides, efforts were taken to couple SnO_2 with other wide energy gap metal oxide with significant improvement in V_{OC}.[23,24] Niinobe et al.[25] explained the improvement in V_{OC} from composite-based photoanode as due to the depression of charge recombination, which contributed to the increment in surface potential and shifted CBM upward. These results indicated that coupling SnO_2 with metal oxide of high CBM and wide energy gap will result in materials of superior properties suitable for high-performance applications, especially photovoltaic. Am-Al_2O_3 meets the candidature requirements. Although am-Al_2O_3 is applied as an insulating material, various studies had shown that Al_2O_3 has surprising advantages in electrical appliances. Coating thin layer of Al_2O_3 on nanoporous TiO_2 demonstrated slower charge recombination rate and large V_{OC},[26] as well as improved photocurrent density due to increase in surface area.[27] However, Zhang et al. reported that further increase in the thickness of Al_2O_3 coating on SnO_2 would decrease the total surface area, which eventually lead to the decrease in photocurrent density.[28] Coating of Al_2O_3 had also showed to passivate surface trap state, thereby leading to better charge transport properties.[29] Al_2O_3 usually exhibits high surface area (>100 m^2/g).[30,31] Sigma et al. reported that well-order α-Al_2O_3 has lower surface area compared to γ-Al_2O_3,[3] indicating that Al_2O_3 with lower crystallinity has higher surface area. Therefore, combining both SnO_2 and am-Al_2O_3 might resulted in composite materials with high conduction band edge, high surface area, and high electron transport properties with improved charge recombination resistance.

Besides, changes in morphology are shown to have significant effects on the materials' performance, especially in their electrical and thermodynamic properties. Compared to smaller nanoparticles, one-dimensional nanostructures such as nanowires and nanofibers, are shown to be beneficial due to their relatively larger volume and thermodynamic stability, with guided charge transport.[32,33] One of the most viable technique to synthesize a variety of one-dimensional materials in large quantities is electrospinning,[34,35] which works under the principle of asymmetric bending of a charged liquid jet in an electric field.

In this study, we have synthesized SnO_2/Al_2O_3 crystal-amorphous hybrid composite material with improved CBM, surface area, and charge recombination resistance via electrospinning a polymeric solution containing Sn and Al precursors and subsequent annealing. Specifically, this article focuses on correlating the surface area and electrical conductivity of electrospun aluminum-doped SnO_2 nanofibers as well as those of a composite nanofiber containing equal molar ratio of SnO_2 and Am-Al_2O_3 (SnO_2/Al_2O_3) to those of pure SnO_2 and Am-Al_2O_3 nanofibers. Advantages of such materials system is also demonstrated by evaluating their performance as DSSC's photoanode. The synthesized samples showed improved surface area, higher conduction band minimum, and suppressed charge recombination with respect to Al%. Surprisingly, despite the similar electrical conductivity of the SnO_2/Al_2O_3 composite fibers to that of pure Am-Al_2O_3, the former demonstrates orders of magnitude higher photocurrent in DSSCs, which is shown to originate from the Fermi energy gradient at the Al_2O_3/SnO_2 interface. The composite nanofiber in the crystalline-amorphous system reported here is expected to have broad implications from their structural and electrical properties.

2 | EXPERIMENTAL DETAILS

2.1 | Nanofibers fabrication

All the chemicals reported in this study were used as received and without further purification. To prepare polymeric solution for electrospinning, a homogeneous mixture of polyvinylpyrrolidone (PVP) (6 g, Mw ~1,300,000, Sigma Aldrich), ethanol (25 ml, absolute, HmbG®), and N'N-dimethylformamide (20 ml, DMF, Emsure®) was prepared in the weight ratio of 13:43.5:43.5. Tin (II) chloride (10 mmol, dihydrate, R&M Chemicals) and aluminum

acetate (10 mmol, basic, R&M Chemicals) were added to the above polymer solution to prepare the electrospinning solutions for SnO_2 and Al_2O_3 nanofibers, respectively. The high molecular weight PVP used in this work helps achieving the required viscosity of electrospinning as well as it avoided hydrolysis of $SnCl_2$. For Al-doped SnO_2, three different Sn/Al molar ratios were used: 95:5, 90:10, and 75:25, which will be denoted as Al(5%), Al(10%), and Al(25%), respectively, throughout this study. To ensure similar electrospinning solution parameters such as viscosity, the total amount of tin (II) chloride and alumina acetate dissolved in the polymeric solution was fixed at 10 mmol in this study. For SnO_2/Al_2O_3 hybrid nanofibers, the Al to Sn precursor ratio was kept at 1:1 keeping the total amount at 10 mmol; this sample will be denoted as Al(50%).The solutions were electrospun using a electrospinning set up (Electroris, Acoulab Pacidic Sdn Bhd) with a potential of 15 kV, flow rate of the solution was set at 0.5 ml/h flow rate and the spacing between the needle tip and collector (aluminum foil) was fixed at ~15 cm. The electrospinning process was carried out at ambient temperature under controlled humidity of ~40%. Obtained nanofibers were then heated at a rate of 2°C/min and calcined at 550°C for 3 hours.

2.2 | Dye-sensitized solar cells fabrication

The DSSCs were assembled as follows. A photoanode paste was prepared by mixing the sample powder (100 mg) with α-terpineol (Sigma Aldrich) and ethyl cellulose (Sigma Aldrich) in 1:4.05:0.5 ratio. Different batches of paste preparation, the amounts of ingredients and ethanol were controlled for consistent concentration and viscosity. DSSCs were fabricated on the fluorine-doped tin oxide-coated glass (FTO) substrate (2.5 cm × 2.5 cm, sheet resistance ~15 Ω/square, Solaronix) was cleaned stepwise using detergent, ethanol, and acetone through ultrasonication. The photoanode paste was then coated on the cleaned FTO-glass using doctor-blade method, applying two layers of scotch tape (Scotch® Magic™ Tape 810, thickness ~0.06 mm) as the spacer; the photoanode-coated FTO was then heated at 500°C for 1 hour. The thickness of the annealed film was measured to be ~15-20 μm. The photoanode film was then soaked in 0.5 mmol/L N3-dye solution overnight, which is prepared by dissolving N3-dye (Dyesol) using tert-butanol (25 ml, EMSURE®) and acetonitrile (25 ml, FISHER) in equivolume ratio. The DSSCs were assembled using a spacer (25 μm, Solaronix), which was placed between the photoanode (working electrode) and commercially available platinum-coated ITO-glass (Solaronix) (counter electrode). Electrolyte (I_3^-/I^-, Solaronix) was filled through orifices developed on the counter electrode. Active area of the prepared DSSCs was ~0.25 cm^2; the electrode area was properly masked to avoid straylight effects during the photovoltaic property determination.

2.3 | Sample and device characterizations

The morphology of the annealed samples was studied using field-emission scanning electron microscope (FESEM, JOEL, JSM-7800F, USA, operating at 30 kV) with sample-emission source distance of 10 mm. The crystal structures of the samples were analyzed using X-ray diffraction (XRD, Bruker, D8 Advance Powder X-ray diffractometer) employing CuK_α radiation (λ = 1.5406 Å); the XRD patterns were recorded in the 10°-80° range in steps of 0.02° at room temperature. Surface chemistry of the samples were analyzed using X-ray photoelectron spectroscopy (XPS, PHI Quantera II, Physical Electronics) employing Al as emission source (λ = 117.4 eV), for both survey (0-1100 eV) and high-resolution scan (480-500 eV, 523-543 eV, and 60-80 eV for Sn, O, and Al core level, respectively). BET surface areas of the samples were studied from N_2 gas adsorption measurements (ASAP2020: Micromeritics Instrument Corporation, USA); the samples were degassed at 200°C before measurements. The energy gaps of the samples were measured using absorption spectroscopy (UV-Vis-NIR Spectrophotometer, UV-2600, Shimazu); thin films developed on glass substrates were scanned between wavelength in the 300-900 nm range employing a scan sampling interval of ~0.5 nm and slit width ~5 nm.

The electrical and electrochemical properties of the samples were studied using linear sweep voltammetry (LSV), cyclic voltammetry, and Mott-Schottky techniques employing PGSTAT M101 with FRA32M module (Methrohm Autolab B.V., the Netherlands). The electrical conductivity of the sample was obtained from LSV by recording the current for a voltage scan of ~0-1 V at a scanning rate of 0.1 V/s and a step potential of 0.00244 V. The cyclic voltammetry was used to measure the oxidation/reduction potentials of the electrode using three-electrode system measurement in 6 mol/L KOH electrolyte using saturated AgCl/Ag and platinum rod as the reference and counter electrodes, respectively. The flat-band potential and carrier concentration of the samples were determined from Mott-Schottky diagram employing electrochemical impedance spectroscopy (EIS). The EIS spectra of the sample were measured from 0.34 to 0.73 V in 0.3 V interval at a frequency range from 100 kHz to 5 mHz. The Mott-Schottky diagram was plotted by fitting the observed impedance, applying the standard Randles circuit using Z view software.

Photovoltaic properties of the fabricated DSSCs were obtained by measuring the *J-V* characteristic under 1 sun illumination, scanning from −0.2 to 0.9 V with 0.02 V/s scanning rate. The impedance of the DSSCs was measured using EIS technique at a frequency range from 100 kHz to 5 mHz. During impedance measurement, the open-circuit voltage of each samples was determined first and applied during measurement to eliminate interference on the results

due to the induced potential within the samples. The delocalized state within band gap was studied by calculating Urbach energy and Stoke shift method using absorption and photoluminescence spectroscopies in dye-anchored samples. Photoluminescence of the dye-anchored samples was measured using a spectrophotometer (NIR 300/2, Edinburgh Instruments) where samples were excited at 600 nm, scanning from 620 to 900 nm with 20 nm bandwidth and 0.5 second dwell time. Absorbance of the dye-anchored samples were measured using absorption spectroscopy (UV-Vis-NIR Spectrophotometer, UV-2600, Shimazu); dye-anchored thin films developed on glass substrates were scanned between wavelength in the 300-900 nm range deploying a scan sampling interval of ~0.5 nm and slit width ~5 nm.

3 | RESULTS AND DISCUSSION

Figure 1 shows the FESEM images of the annealed samples synthesized in the present study; they showed nanofiber morphology with an average fiber diameter of < 100 nm and with a high degree of diameter uniformity. The diameter of the fibers, as tabulated in Table 1, decreased with the increase in the Al content on an average, which is likely due to the difference in ionic sizes of Sn (0.69 Å) and Al (0.53 Å).[36] The smaller Al ion has higher charge density and would impose larger force of elongation on the fibers, resulting in smaller fiber diameter.[37] FESEM images of both Al(25%) and Al(50%) samples showed clusters on the nanofiber surface, which could be explained according to Hume-Rothery rules on the requirements of solute dissolution in a solid solution: (a) difference in atomic radius <15%, (b) similar crystal structure, (c) similar ion valency, and (d) similar electronegativity.[38] These requirement were not met in the present case, suggesting limited solubility of Al in SnO_2 lattice; however, owing to a difference of ~23% between the sizes of the Sn and Al ions, a large fraction of Al ion could occupy the interstitial positions.

Figure 2 shows the XRD patterns of the annealed samples revealing sharp peaks at 26° (110), 34° (101), and 52° (221); which can be indexed to Rutile SnO_2 (tetragonal), consistent with the values given in the standard card

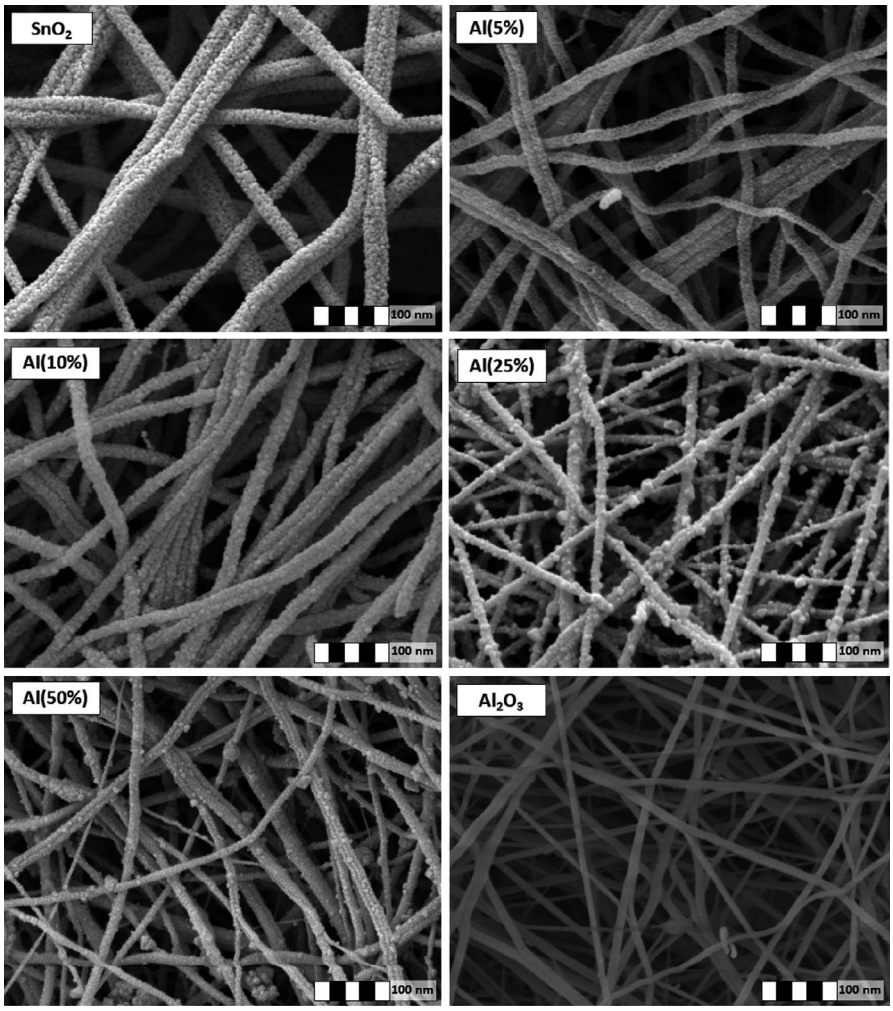

FIGURE 1 Nanofibers morphology of synthesized samples

TABLE 1 The viscosity of electrospinning solution. The nanofiber average diameter, crystal parameter, surface area characteristic, and electrical conductivity of the samples

Sample	Viscosity (cP)	Diameter (nm)	Lattice parameter (Å)		BET area (m^2/g)	Pore size (Å)	σ (nS/cm)
			$a = b$	c			
SnO_2	—	94.6 ± 15.3	4.73	3.18	35.6	385.9	10.84
Al(5%)	219	90.2 ± 9.7	4.73	3.17	49.3	264.6	9.89
Al(10%)	—	90.9 ± 8.9	4.72	3.18	54.9	238.0	4.01
Al(25%)	—	80.7 ± 13.9	4.72	3.18	56.8	150.8	2.30
Al(50%)	207	82.6 ± 11.4	4.72	3.17	58.0	132.8	0.97
Al_2O_3	191	79.8 ± 10.6	Amorphous		201.9	115.4	0.91

(JCPDS 41-1445). The lattice parameters were calculated to be $a = b$ ~4.735 Å and c ~ 3.177 Å, similar to the values reported in previous studies on pure SnO_2.[39] Absence of metallic Sn peak at ~31° (111) suggest complete oxidation of all samples;[40] whereas no peaks corresponding to any phase of Al_2O_3 was observed, thereby indicating that Al_2O_3 is amorphous due to low calcination temperature (550°C).[4] Detailed analysis on the XRD of these samples (Figure 2 and Table S1) showed a small shift in the diffraction peak (0.04°) to higher angles with peak broadening for Al(5%) and Al(10%), suggesting straining of the unit cell due to Al ions occupancy within the crystal. However, for the Al(25%) sample, the diffraction peak showed no shift and no broadening with respect to SnO_2; suggesting that doping has not occurred in this case. The FESEM images of this sample showed formation of clusters on the surface, which according to EDX analysis (Figure S1) is Al-rich clusters. Further increase in the Al content, ie, the Al(50%) sample, resulted in Al-rich secondary phase formation on the nanofiber surface. Interestingly, a peak shift (0.05°) occurred in the Al(50%) indicating partial doping and partial precipitation.

For a detailed surface chemistry characterization of the pure and the composite fibers, XPS analyses have been carried out; results of which are shown in Figure 3. The XPS survey scan shown in Figure 3A, confirmed the presence of Al_2O_3 and SnO_2; the Al 2p core level shown in Figure 3B revealed an increase in peak intensity with increasing Al content thereby confirming higher Al addition in the sample. Therefore, absence of diffraction peaks corresponding to Al_2O_3 in the XRD pattern of the composite fibers and presence of Al in the XPS results concluded a crystal-amorphous SnO_2/Al_2O_3 hybrid composite. The binding energy of Al 2p increased from 73 to 75.4 eV (Table S2) as the Al content increased from 5 to 50 mol%, indicating orbital changes from 2p1/2 to 2p3/2. Lower binding energy of Al 2p in the sample with Al content <25 mol% could be due to the bonding with Sn, which results from Al doping in SnO_2 crystal, whereas 75.4 eV binding energy for Al content >25 mol% can be designated to the Al-O bonding in Al_2O_3 structure. The Sn 3d core level, Figure 3C, displayed two high intensity peaks at ~485 and ~494 eV for $3d_{5/2}$ and $3d_{3/2}$, respectively, deducing that Sn species in all samples presented in Sn (IV) state, the usual oxidation state for SnO_2.[41] Once again, sample with Al content <25 mol% showed lower binding energy mainly due to Sn–Al bonding within the SnO_2 crystal structure. Sn core level of Al(50%) show distinctive peak at higher binding energy (496.8 eV compared to 493.5 eV) with another small deconvoluted peak at lower binding energy indicating small degree of Al-doping within the SnO_2 crystal structure. The O1s core level spectra, Figure 3D, can be deconvoluted into two peaks with slightly different binding energies, ~528.8 and

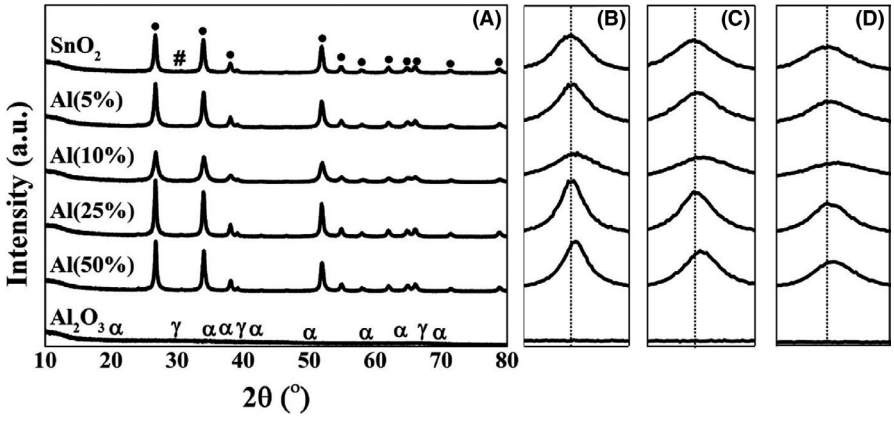

FIGURE 2 (A) XRD spectra of all samples where • represented SnO_2 peak, # the Sn peak, α and γ the α-Al_2O_3, and γ-Al_2O_3 peak, respectively, as well as peak shifting for (B) [1 1 0], (C) [1 0 1], and (D) [2 1 1] plane

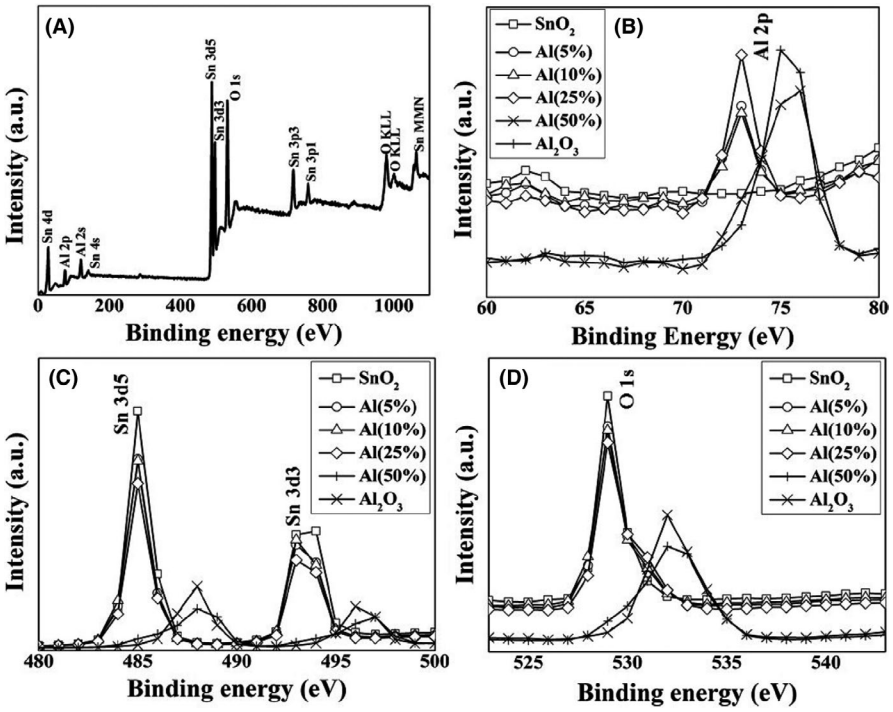

FIGURE 3 XPS results of (A) SnO_2/Al_2O_3 composite survey scan, together with core level scanning of (B) Al 2p, (C) Sn 3d, and (D) O 1s species

~530.3 eV, corresponding to Sn–O–Sn,[42] and Sn–O–Al or Al–O–Al[43] bonding, respectively. BE for Sn, Al, and O core level were tabulated in Table S2. This assignment is because Al-bonded electron will have higher binding energy due to its smaller atomic size. Thus, the XPS measurement corroborate the XRD and EDX results that the samples are composite-like structures with partial doping of Al in SnO_2 in the main fibrous structure, which is covered by Al_2O_3 rich particles.

Effect of increasing Al content on the surface area of the sample was carried out through gas adsorption studies and determining the BET surface area measurement. BET analysis (Table 1) showed increase in the surface area of the sample with increase in the Al content. The BET isotherm plots (Figure S2) showed type IV irreversible isotherms and hysteresis during absorption-desorption, resulting from capillary condensation in a nanoscale cavity at pressure lower than the saturation pressure.[44] The results suggested interconnected pores structure, and the surface porosity of the samples changed from macroporous to mesoporous with increase in the Al content.

Similar to its effect on the surface area, incorporation of Al would affect the electrical properties of the samples also. Linear sweep voltammetry (LSV) were carried out to analyze the electrical properties of the samples. The LSV concluded that the conductivity of the samples, summarized in Figure 4, decreased with an increase in the Al content, from 1.1×10^{-8} S/cm for SnO_2[45] to 0.9×10^{-10} S/cm for Al_2O_3 (Table 1).[46] One of the motivations for synthesizing a composite containing equal mole fraction of SnO_2 and Al_2O_3. That is, Al(50%) was used to develop a material with similar electrical conductivity as that of SnO_2 and similar BET surface area as that of Al_2O_3. We have recently successfully developed composite ceramic nanowires with a similar strategy but focusing on different properties (such as combining electrochemical activity and electrical conductivity, etc.) for energy conversion and storage applications.[35,47–50] However, the present crystal/amorphous composite does not show the anticipated properties; the electrical conductivity of the Al(50%) was rather similar to that of pure am-Al_2O_3. Despite the inferior electrical conductivity of Al(50%), the sample showed interesting photoelectric properties as detailed subsequently.

The current density-voltage curves of the fabricated DSSCs are shown in Figure 5 and the corresponding photovoltaic parameters are listed in Table 2. Both Al(5%) and

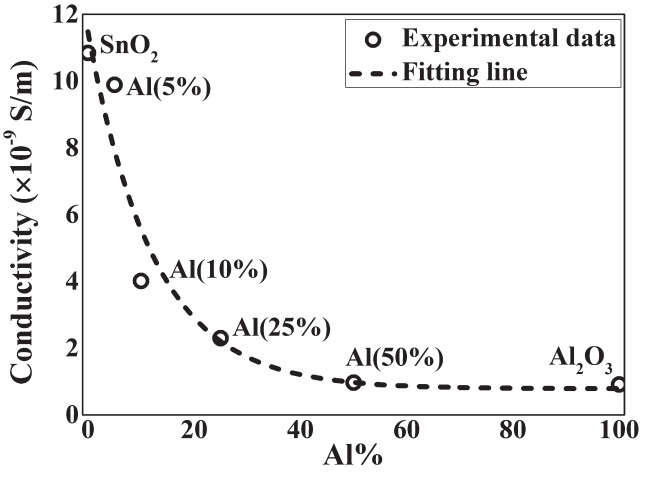

FIGURE 4 Electrical conductivity of samples with respect to the Al% measured using linear sweep voltammetry

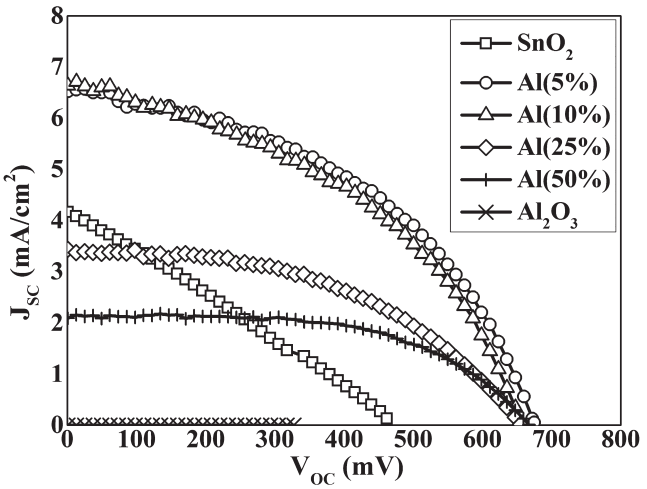

FIGURE 5 Photovoltaic performance of fabricated DSSCs

Al(10%) samples showed higher photocurrent than SnO_2 (Table 2), source of which could be analyzed using a simple model of one-dimensional current density of an electronic device is given by:

$$J(x) = n(x)\,\mu(x)\,\nabla F \tag{1}$$

where $n(x)$ is the electron density, $\mu(x)$ is the charge mobility, and ∇F is the gradient in Fermi energy between the materials interface. The open circuit voltage (V_{OC}) of DSSCs is proportional to this gradient in Fermi energy, ie, increase in the photocurrent is followed by an increase in the voltage. The photocurrent systematically lowered with an increase in Al content; interestingly, despite the similar electrical conductivity of Al(50%) as that of am-Al_2O_3, the former gave orders of magnitude higher photocurrent. The source of this enhancement is systematically investigated by measuring the charge transport and device physical parameters using electrochemical impedance spectroscopy (Table 2) and discussed subsequently.

The electron transport resistance (R_S) increased with an increase in the Al content (Table 2), which is consistent with the LSV data in Figure 5 and would explain the lowering of current density in Figure 5. Similar with previous studies, the charge recombination resistance (R_{CR}) was increased by incorporating large band gap metal oxide,[26,27,51] which in this case in Al_2O_3. Using the transmission line model developed by Bisquert et al,[52] electron lifetime (τ_n), electron diffusion coefficient (D_n), and electron transport time (τ_d) were calculated from the EIS results and shown in Table 2. The electron lifetime of the sample increased with an increase in the Al content, which is up to fourfold for the Al(25%) sample. This increase in electron lifetime could be attributed to the increase in R_{CR}.[51] However, the electron transport time (the time required to reach the electrode) of the samples increased due to the higher sample resistivity, whereas the diffusion coefficient decreased with an increase in the Al content, both indicating the decrease in the electron transport properties of the sample, which is likely due to the defects in SnO_2 crystal upon Al-doping and Al_2O_3 incorporation.[53]

In nanomaterials, slow electron diffusion has been related to the localized energy states within the band gap as a result of poor crystallinity.[54] This issue has been addressed by coupling absorption and photoluminescence spectroscopies and evaluated trap states via Urbach energy (E_U) and Stoke shift. The energy gap of the samples was calculated from the absorption spectra via Tauc's plot technique, showing narrowing energy gap, from 3.7 to 3.4 eV[7] for SnO_2 and Al_2O_3, respectively (Figure 6). In consistent with the XRD analyses, ie, partial doping has occurred in the samples other than Al(25%), a lowering of energy gap was observed in the corresponding samples. Ideally, absorption coefficient of highly crystalline materials shows a single exponential curve; however, due to defects and energy traps, a multi-exponential curve is routinely observed, as seen in Figure 6. The calculated E_U of the materials is shown in Table 3, which demonstrates that E_U generally increased upon Al addition as a result of delocalized states within the energy gap. These states trap electrons in the conduction band by providing alternative route with lower energies, which cause the electrons to degenerate via photon relaxation into the trap state. Such degeneration can be observed from a Stoke shift (Figure S3, measured using the dye-anchored electrodes), which measures the difference between lowest absorbed and

TABLE 2 The electrical properties and photovoltaic performance of the samples. τ_n, D_n, and τ_d are the electron lifetime, diffusion coefficient, and transport respectively, E_U the Eubach energy

Sample	V_{OC} (mV)	J_{SC} (mA/cm^2)	FF	η (%)	R_S (Ω)	R_{CT} (kΩ)	R_{CR} (MΩ)	τ_n (ms)	D_n (cm^2/s)	τ_d (s)
SnO_2	462.04	4.168	27.8	0.54	82	0.03	0.05	5.4	1.4×10^{-5}	0.003
Al(5%)	674.65	6.526	46.0	2.03	150	0.3	0.40	6	1.1×10^{-5}	0.004
Al(10%)	657.47	6.635	43.6	1.90	92	1	0.65	13	2.0×10^{-6}	0.02
Al(25%)	655.06	3.437	47.4	1.07	255	10	2.00	22	3.6×10^{-7}	0.11
Al(50%)	667.24	2.089	58.9	0.82	130	80	1.30	19.5	3.3×10^{-8}	1.2
Al_2O_3	327.70	0.013	40.0	0.002	350	80	0.67	10.1	3.3×10^{-8}	1.2

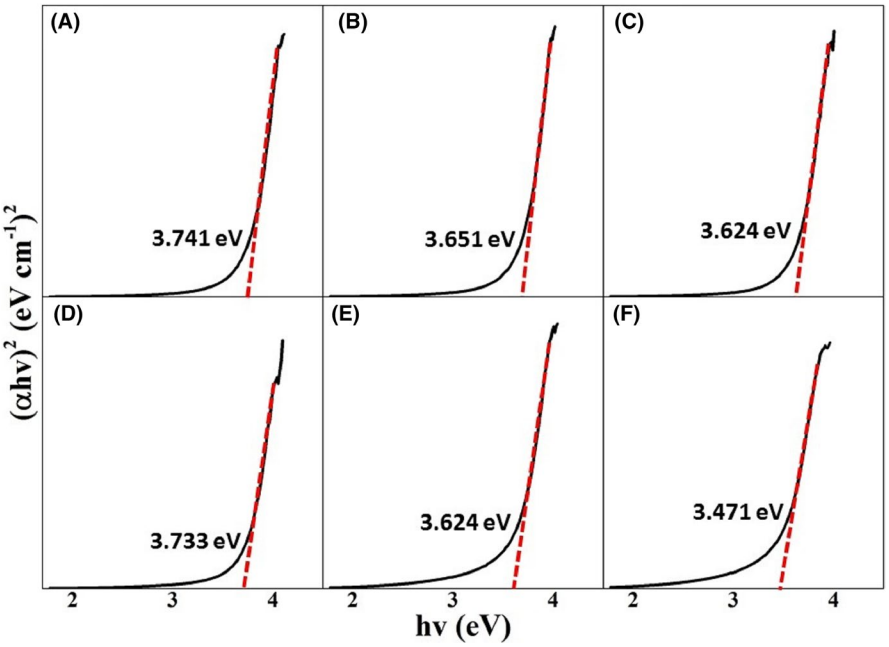

FIGURE 6 Tauc's plot of (A) SnO_2, (B) Al(5%), (C) Al(10%), (D) Al(25%), (E) Al(50%), and (F) Al_2O_3 nanofibers, respectively, showing high absorption at high energy photon region [Color figure can be viewed at wileyonlinelibrary.com]

emitted photon energy. The Stoke shift shown in Table 3 reveal larger loss in photon energy with an increase in the Al content, which is most likely due to the degeneration of deeper energy traps with an increase in the Al content (as schematically shown in Figure S4), dragging the electrons collection efficiency.

As discussed, electrochemical impedance spectroscopy showed a decrease in electron diffusion coefficient and charge mobility ($\mu(x)$) with an increase in the Al content; whereas the gas adsorption studies showed that the surface area was increased with an increase in the Al content. The latter improvement increased the binding site for dye molecules, generating higher concentration of carriers, which was further confirmed using Mott-Schottky technique (Table 3). Both Al(5%) and Al(10%) samples showed higher carrier concentration compared to the loss in charge mobility, thereby resulting in improved current density. With higher Al content (Al > 10%), the losses in charge mobility is too large to be compensated by the increase in carrier concentration and current density decreases compared to SnO_2.

Incorporation of Al offered improved open-circuit voltage (V_{OC}) compared to SnO_2; the V_{OC} of the DSSCs is determined by the CBM of the photoanode and electrochemical potential of the electrolyte.[55] Considering similar electrolyte used in DSSCs fabrication, the improvement in the V_{OC} is thereby attributed mostly to the position of the CBM of the sample when Al was incorporated.[29] The Schottky barrier, also known as flat-band potential, was used to study the position of CBM of the samples. Mott-Schottky plot (Figure S5) showed an increase in the flat-band potential as compared to SnO_2 (Table 3) indicating increase in CBM of the sample with respect to the metal contact. This result was consistent with the cyclic voltammetry analysis of the samples (Figure S6), where negative shift in the anodic oxidation peak was observed, which could be indicating a possible upward shift in the CBM energy. The presence of secondary anodic peak in the CV curve (Figue S6) also highlight the presence of delocalized state below the conduction band. Measurement of the LSV ON voltage provides an alternative to study the flat-band potential. During

TABLE 3 The impedance, dye concentration, and carrier concentration of the DSSCs as well as flat-band potential (E_{fb}) and carrier concentration (N_d) of the bare samples

Sample	C_{dye} (mmol/cm^2)	N_d-cell (m^{-3})	E_U (eV)	Stoke's Shift (nm)	E_{fb} (V)	On voltage (mV)	N_d (m^{-3})
SnO_2	0.80	3.3×10^7	0.40	13.95	−0.0544	347.30	740.0
Al(5%)	1.09	5.1×10^8	0.41	14.92	−0.1334	341.76	303.7
Al(10%)	1.33	2.5×10^8	0.42	13.42	−0.3576	326.76	47.9
Al(25%)	1.42	8.4×10^8	0.43	18.48	−0.3361	351.35	241.6
Al(50%)	1.50	2.2×10^9	0.52	24.03	−0.3452	351.75	113.0
Al_2O_3	1.66	$1.9 \times \times 10^9$	0.56	28.52	−0.3482	398.31	116.0

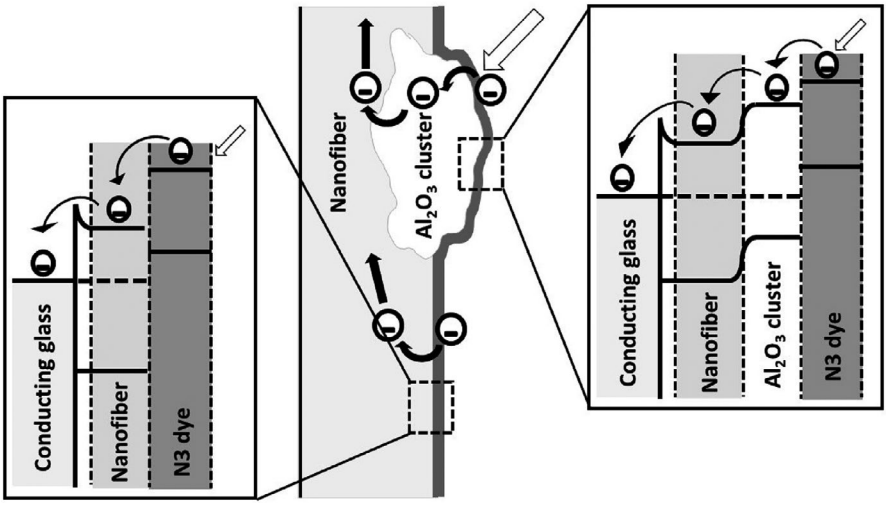

FIGURE 7 Electron flow from dye-molecules to nanofiber directly, or via Al_2O_3 cluster. Rectifying behavior can be observed in the metal-semiconductor interface, where band-bending at cluster nanofiber interface due to the difference in Fermi energy level

forward bias, charges accumulate, thereby raising the Fermi energy level; at sufficiently applied potential (ON voltage), the Schottky barrier is surpassed, and an upsurge of current is recorded. The On voltage decreased for Al(25%) but increased for the Al(25%) sample, indicating narrowing and widening of Schottky barrier on these samples, respectively (Table 3 and Figure S7). This behavior could be explained by the changes in the Fermi energy level of the samples, which is largely affected by the carrier concentration. The carrier concentration of the samples was calculated from the slope of the Mott-Schottky analysis; the carrier concentration sharply decreased from ~740 m^{-3} (SnO_2) to ~48 m^{-3} (Al 10%), ie, an order of magnitude, indicating a N-type to P-type semiconductor transition.[56] As a result, the Fermi energy descends nearer to valence band, thereby negatively shifting the CBM as well as narrowing the Schottky barrier as illustrated in Figure S8. At Al content >25 mol%, the carrier concentration of the samples is higher than that of Al(10%) and the CBM of the samples is positively shifted with wider Schottky barrier for both Al(25%) and Al(50%) samples. The shifting of Fermi energy due to the carrier concentration thereby explain the drop in flat-band potential for sample with Al content >25 mol%. The increase in CBM energy might affect the electron injection rate from the excited dye to the photoanode.[57,58] The results showed that the V_{OC} of the DSSCs is directly affected by the flat-band potential, indicating that the drag of injection rate is negligible with CBM playing the most crucial part in V_{OC} determination.

Besides the movement of CBM with Al content, higher charge recombination resistance observed in such samples also contributed to improved V_{OC}.[59] EIS analysis on the DSSCs showed improved charge recombination resistance with an increase in the Al content (Table 2). Higher charge recombination resistance also contributed to increase in the fill factor.[60] The decrease in the charge recombination resistance of Al_2O_3 compared to Al(50%) resulted from the energy traps. The Urbach energy measurement showed that Al_2O_3 has the deepest delocalized energy trap state as it is amorphous, indicating that electrons in the conduction band degenerate thermally into the trap state. Within the trap state, the electron prone toward recombination with either the electrolyte or holes in the valence band of the samples, therefore, increasing the electrons recombination rate (Figure S4).

Finally, we comment on the origin of higher photocurrent in Al(50%) despite its similar electrical conductivity as that of am-Al_2O_3. Compared to am-Al_2O_3, Al-rich cluster formation on Al(50%) nanofiber was verified via FESEM and EDX analysis, which generated two regions with different electronic structure; am-Al_2O_3 cluster of lower Fermi energy and SnO_2 nanofibers of higher Fermi energy. When these materials are in contact, the Fermi energy level is realigned thereby resulting in a band bending at the cluster-nanofiber as illustrated in Figure 7. According to Equation 1, current density is directly proportional to the Fermi energy gradient. The band-bending in Al(50%) cluster-nanofiber interface could facilitate the flow of electrons. Such characteristic was absent in am-Al_2O_3 nanofibers. Therefore, albeit having similarly low electrical conductivity, Al(50%) has higher carrier concentration, charge mobility and Fermi energy gradient compared to Al_2O_3, thereby leading to the order of magnitude for better photovoltaic performance. These observations would have considerable practical implications. For example, the SnO_2/Al_2O_3 composite offers improved charge recombination resistance without the need of multiple-step deposition techniques, such as coating, and serve as promising materials for applications such as photovoltaic, energy storage, and gas sensor. Formation of cluster on the nanofiber surface arise interesting electrical behavior, like band bending which facilitated the flow of electron. This study also opens new opportunities in studying the structure-property correlations in amorphous-crystalline materials composites.

4 | CONCLUSIONS

To conclude, we prepared crystal-amorphous SnO_2/Al_2O_3 hybrid nanofibers via electrospinning. We noted that Al-doping occurred at low Al content (Al < 10%), where precipitation occurred at higher Al content (Al > 25%). Due to low solubility limit, aggregates of Al could be observed in the form of cluster on the nanofiber surface. The incorporation of Al_2O_3 within SnO_2 improved the surface area of the samples, however, at the expense of electrical conductivity, where increase in charge transport resistance was recorded by EIS analysis. Based on the optical investigation, energy traps generated by defect, which resulted from lower crystallinity, is responsible for the deterioration of charge mobility. The 5 and 10 mol% Al containing SnO_2 sample showed higher photocurrent and open circuit voltage compared to its pure analogues; subsequent addition deteriorated the properties. Increase in photocurrent has been shown to result from a trade-off between surface area and electrical conductivity, ie, the gain in photocurrent through an increase in carrier concentration by increasing surface area (thereby dye-loading) was higher than the loss in photocurrent due to poor conductivity. The Al containing SnO_2 showed improved V_{OC} by increasing the CBM energy level as well as charge recombination resistance. Orders of magnitude higher photocurrent was observed in a sample containing equal mol% am-Al_2O_3 and SnO_2 than pure am-Al_2O_3 despite their similar electrical conductivity, which is shown to originate from a band-bending at the am-Al_2O_3 cluster-SnO_2 nanofiber interface.

ACKNOWLEDGMENT

The authors acknowledged funding from Flagship Leap 3 research grant (RDU172201) of Universiti Malaysia Pahang (http://www.ump.edu.my).

ORCID

Rajan Jose https://orcid.org/0000-0003-4540-321X

REFERENCES

1. Lu H, Li Q, Su G, Zheng M, Zhao Y, Miao X, et al. Synthesis of three crystalline forms of Al_2O_3 featuring rod-like fibers and their effect on the gaseous degradation of 1-chloronaphthalene. Environmental Science: Nano. 2017;4(5):994–1004.
2. Ponja SD, Parkin IP, Carmalt CJ. Synthesis and material characterization of amorphous and crystalline (α-) Al_2O_3 via aerosol assisted chemical vapour deposition. RSC Adv. 2016;6(105):102956–60.
3. Singh S, Srivastava VC, Mandal TK, Mall ID. Synthesis of different crystallographic Al_2O_3 nanomaterials from solid waste for application in dye degradation. RSC Adv. 2014;4(92):50801–10.
4. Tavakoli AH, Maram PS, Widgeon SJ, Rufner J, van Benthem K, Ushakov S, et al. Amorphous alumina nanoparticles: structure, surface energy, and thermodynamic phase stability. J Phys Chem C. 2013;117(33):17123–30.
5. Cheng B, Tian B, Xie C, Xiao Y, Lei S. Highly sensitive humidity sensor based on amorphous Al_2O_3 nanotubes. J Mater Chem. 2011;21(6):1907–12.
6. Rose V, Franchy R. The band gap of ultrathin amorphous and well-ordered Al_2O_3 films on CoAl(100) measured by scanning tunneling spectroscopy. J Appl Phys. 2009;105(7):07C902.
7. Costina I, Franchy R. Band gap of amorphous and well-ordered Al_2O_3 on $Ni_3Al(100)$. Appl Phys Lett. 2001;78(26):4139–41.
8. Filatova EO, Konashuk AS. Interpretation of the changing the band gap of Al_2O_3 depending on its crystalline form: connection with different local symmetries. J Phys Chem C. 2015;119(35):20755–61.
9. Sankaran K, Pourtois G, Degraeve R, Zahid MB, Rignanese G-M, Houdt JV. First-principles modeling of intrinsic and extrinsic defects in γ-Al_2O_3. Appl Phys Lett. 2010;97(21):212906.
10. Ealet B, Elyakhloufi MH, Gillet E, Ricci M. Electronic and crystallographic structure of γ-alumina thin films. Thin Solid Films. 1994;250(1):92–100.
11. Yazdanmehr M, Asadabadi SJ, Nourmohammadi A, Ghasemzadeh M, Rezvanian M. Electronic structure and bandgap of γ-Al_2O_3 compound using mBJ exchange potential. Nanoscale Res Lett. 2012;7(1):488.
12. TardíoMM, RamírezR, GonzálezR, et al. Enhancement of electrical conductivity in α-Al_2O_3 crystals doped with magnesium. J Appl Phys. 2001;90(8):3942–51.
13. Jo C-H, Jo J-H, Myung S-T. Confinement of nanosized tin(IV) oxide particles on rGO sheets and its application to sodium-ion full cells as a high capacity anode material. J Alloy Compd. 2018;731:339–46.
14. Bendjedidi H, Attaf A, Saidi H, Aida MS, Semmari S, Bouhdjar A, et al. Properties of n-type SnO_2 semiconductor prepared by spray ultrasonic technique for photovoltaic applications. J Semiconductors. 2015;36(12):123002.
15. Singh AK, Janotti A, Scheffler M, Van de Walle CG. Sources of electrical conductivity in SnO_2. Phys Rev Lett. 2008;101(5):055502.
16. Balzarotti A, Bianconi A. Electronic structure of aluminium oxide as determined by X-Ray photoemission. Physica Status Solidi (b). 1976;76(2):689–94.
17. Zhou W, Liu Y, Yang Y, Wu P. Band gap engineering of SnO2 by epitaxial strain: experimental and theoretical investigations. J Phys Chem C. 2014;118(12):6448–53.
18. Li GJ, Kawi S. High-surface-area SnO_2: a novel semiconductor-oxide gas sensor. Mater Lett. 1998;34(1):99–102.
19. Wali Q, Fakharuddin A, Ahmed I, Ab Rahim MH, Ismail J, Jose R. Multiporous nanofibers of SnO_2 by electrospinning for high efficiency dye-sensitized solar cells. J Mater Chem A. 2014;2(41):17427–34.
20. Birkel A, Lee Y-G, Koll D, Meerbeek XV, Frank S, Choi MJ, et al. Highly efficient and stable dye-sensitized solar cells based on SnO_2 nanocrystals prepared by microwave-assisted synthesis. Energy Environ Sci. 2012;5(1):5392–400.
21. Basu K, Benetti D, Zhao H, Jin L, Vetrone F, Vomiero A, et al. Enhanced photovoltaic properties in dye sensitized solar cells by surface treatment of SnO_2 photoanodes. Sci Rep. 2016;6:23312.
22. Sasidharan S, Soman S, Pradhan SC, Unni KNN, Mohamed AAP, Nair BN, et al. Fine tuning of compact ZnO blocking layers for

enhanced photovoltaic performance in ZnO based DSSCs: a detailed insight using β recombination, EIS, OCVD and IMVS techniques. New J Chem. 2017;41(3):1007–16.

23. Wang D, Wu C, Luo W, Guo X, Qu B, Xiao L, et al. ZnO/SnO_2 double electron transport layer guides improved open circuit voltage for highly efficient $CH_3NH_3PbI_3$-based planar perovskite solar cells. ACS Appl Energy Mater. 2018;1(5):2215–21.
24. Mao X, Zhou R, Zhang S, Ding L, Wan L, Qin S, et al. High efficiency dye-sensitized solar cells constructed with composites of TiO_2 and the hot-bubbling synthesized ultra-small SnO_2 nanocrystals. Sci Rep. 2016;6:19390.
25. Niinobe D, Makari Y, Kitamura T, Wada Y, Yanagida S. Origin of enhancement in open-circuit voltage by adding ZnO to nanocrystalline SnO_2 in dye-sensitized solar cells. J Phys Chem B. 2005;109(38):17892–900.
26. Palomares E, Clifford JN, Haque SA, Lutz T, Durrant JR. Control of charge recombination dynamics in dye sensitized solar cells by the use of conformally deposited metal oxide blocking layers. J Am Chem Soc. 2003;125(2):475–82.
27. Seok Cheol C, Ho Suk L, Sang Jin O, Sang Ho S. Light scattering TiO_2 particles surface-modified by Al_2O_3 coating in a dye-sensitized solar cell. Phys Scr. 2012;85(2):025801.
28. Zhang X-T, Sutanto I, Taguchi T, Tokuhiro K, Meng Q-B, Rao TN, et al. Al_2O_3-coated nanoporous TiO_2 electrode for solid-state dye-sensitized solar cell. Sol Energy Mater Sol Cells. 2003;80(3):315–26.
29. Prasittichai C, Hupp JT. Surface modification of SnO_2 photoelectrodes in dye-sensitized solar cells: significant improvements in photovoltage via Al_2O_3 atomic layer deposition. J Phys Chem Lett. 2010;1(10):1611–5.
30. Hu F, Wu X, Wang Y, Lai X. Ultrathin γ-Al_2O_3 nanofibers with large specific surface area and their enhanced thermal stability by Si-doping. RSC Adv. 2015;5(67):54053–8.
31. Comet M, Schreyeck-Reinert L, Louis C, Fuzellier H. Synthesis and characterization of high surface area aluminium and alumina microtubes from carbonaceous materials. J Mater Chem. 2002;12(3):754–7.
32. Zhou Y, Liu L, Wu T, Yuan G, Li J, Ding Q, et al. Flake-like $InVO_4$ modified TiO_2 nanofibers with longer carrier lifetimes for visible-light photocatalysts. RSC Adv. 2018;8(48):27073–9.
33. Mukherjee K, Teng T-H, Jose R, Ramakrishna S. Electron transport in electrospun TiO_2 nanofiber dye-sensitized solar cells. Appl Phys Lett. 2009;95(1):012101.
34. Shi J, You T, Gao Y, Liang X, Li C, Yin P. Large-scale preparation of flexible and reusable surface-enhanced Raman scattering platform based on electrospinning AgNPs/PCL nanofiber membrane. RSC Adv. 2017;7(75):47373–9.
35. Pal B, Bakr ZH, Krishnan SG, Yusoff MM, Jose R. Large scale synthesis of 3D nanoflowers of SnO_2/TiO_2 composite via electrospinning with synergistic properties. Mater Lett. 2018;225:117–21.
36. Shannon R. Revised effective ionic radii and systematic studies of interatomic distances in halides and chalcogenides. Acta Crystallographica Sec A. 1976;32(5):751–67.
37. Pillay V, Dott C, Choonara YE, Tyagi C, Tomar L, Kumar P, et al. A review of the effect of processing variables on the fabrication of electrospun nanofibers for drug delivery applications. J Nanomater. 2013;2013:1–22.
38. Hume-Rothery W, Mabbott GW, Evans KMC. The freezing points, melting points, and solid solubility limits of the alloys of sliver and copper with the elements of the b sub-groups. Philos Trans R Soc London Ser A, Containing Papers Mathematical or Physical Character. 1934;233(721–730):1.
39. Shi L, Lin H. Facile fabrication and optical property of hollow SnO_2 spheres and their application in water treatment. Langmuir. 2010;26(24):18718–22.
40. Oehl N, Schmuelling G, Knipper M, Kloepsch R, Placke T, Kolny-Olesiak J, et al. In situ X-ray diffraction study on the formation of α-Sn in nanocrystalline Sn-based electrodes for lithium-ion batteries. Cryst Eng Comm. 2015;17(44):8500–4.
41. Ahn H-J, Choi H-C, Park K-W, Kim S-B, Sung Y-E. Investigation of the structural and electrochemical properties of size-controlled SnO_2 nanoparticles. J Phys Chem B. 2004;108(28):9815–20.
42. Jeong J, Lee BJ. X-ray photoelectron spectroscopy study of SnO_2 and SnO_{2+x} thin films. J Nanosci Nanotechnol. 2013;13(1):711–3.
43. Strohmeier BR. Gamma-alumina (γ-Al_2O_3) by XPS. Surf Sci Spectra. 1994;3(2):135–40.
44. Haul RSJ, Gregg KSW, Sing: adsorption, surface area and porosity. 2. Auflage, Academic Press, London 1982. 303 Seiten, Preis: $ 49.50. Berichte der Bunsengesellschaft für physikalische Chemie. 1982;86(10):957–957.
45. Yakuphanoglu F. Electrical conductivity, Seebeck coefficient and optical properties of SnO_2 film deposited on ITO by dip coating. J Alloy Compd. 2009;470(1):55–9.
46. El-Shaarawy MG, Bayoumy WAA. Doping effect on the electrical properties of amorphous Al_2O_3. Mater Chem Phys. 2003;78(2):405–11.
47. Bakr ZH, Wali Q, Yang S, Yousefsadeh M, Padmasree KP, Ismail J, et al. Characteristics of ZnO-SnO_2 composite nanofibers as a photoanode in dye-sensitized solar cells. Ind Eng Chem Res. 2019;58(2):643–53.
48. Harilal M, Krishnan SG, Vijayan BL, Venkatashamy Reddy M, Adams S, Barron AR, et al. Continuous nanobelts of nickel oxide–cobalt oxide hybrid with improved capacitive charge storage properties. Mater Des. 2017;122:376–84.
49. Pal B, Vijayan BL, Krishnan SG, Harilal M, Basirun WJ, Lowe A, et al. Hydrothermal syntheses of tungsten doped TiO_2 and TiO_2/WO_3 composite using metal oxide precursors for charge storage applications. J Alloy Compd. 2018;740:703–10.
50. Vijayan BL, Krishnan SG, Zain NKM, Harilal M, Yar A, Misnon II, et al. Large scale synthesis of binary composite nanowires in the Mn_2O_3-SnO_2 system with improved charge storage capabilities. Chem Eng J. 2017;327:962–72.
51. Archana PS, Gupta A, Yusoff MM, Jose R. Charge transport in zirconium doped anatase nanowires dye-sensitized solar cells: trade-off between lattice strain and photovoltaic parameters. Appl Phys Lett. 2014;105(15):153901.
52. Bisquert J, Fabregat-Santiago F, Mora-Seró I, Garcia-Belmonte G, Giménez S. Electron lifetime in dye-sensitized solar cells: theory and interpretation of measurements. J Phys Chem C. 2009;113(40):17278–90.
53. Finetti M, Galloni R, Mazzone AM. Influence of impurities and crystalline defects on electron mobility in heavily doped silicon. J Appl Phys. 1979;50(3):1381–5.
54. Kerr CS, Kryukovskiy A, Chen JIL. Effects of surface passivation on trap states, band bending, and photoinduced charge transfer in P3HT/TiO_2 hybrid inverse opals. J Phys Chem C. 2018;122(30):17301–8.

55. Pradhan SC, Hagfeldt A, Soman S. Resurgence of DSCs with copper electrolyte: a detailed investigation of interfacial charge dynamics with cobalt and iodine based electrolytes. J Mater Chem A. 2018;6(44):22204–14.
56. Benouis CE, Benhaliliba M, Mouffak Z, Avila-Garcia A, Tiburcio-Silver A, Ortega Lopez M, et al. The low resistive and transparent Al-doped SnO_2 films: p-type conductivity, nanostructures and photoluminescence. J Alloy Compd. 2014;603:213–23.
57. Shaikh JS, Shaikh NS, Mali SS, Patil JV, Pawar KK, Kanjanaboos P, et al. Nanoarchitectures in dye-sensitized solar cells: metal oxides, oxide perovskites and carbon-based materials. Nanoscale. 2018;10(11):4987–5034.
58. Zannotti M, Wood CJ, Summers GH, Stevens LA, Hall MR, Snape CE, et al. Ni Mg mixed metal oxides for p-type dye-sensitized solar cells. ACS Appl Mater Interfaces. 2015;7(44):24556–65.
59. Zhang H, Chen Z, Hu R, Liu J, Cui J, Zhou W, et al. Enabling a highly reversible conversion reaction in a lithiated nano-SnO_2 film coated with Al_2O_3 by atomic layer deposition. J Mater Chem A. 2018;6(10):4374–85.
60. Bartesaghi D, Pérez IdC, Kniepert J, Roland S, Turbiez M, Neher D, et al. Competition between recombination and extraction of free charges determines the fill factor of organic solar cells. Nature. Communications. 2015;6:7083.

SUPPORTING INFORMATION

Additional supporting information may be found online in the Supporting Information section at the end of the article.

How to cite this article: JinKiong L, Pal B, Chong K, Schmidt-Mende L, Bisquert J, Jose R. Photocurrents in crystal-amorphous hybrid stannous oxide/alumina binary nanofibers. *J Am Ceram Soc*. 2019;102:6337–6348. https://doi.org/10.1111/jace.16504